Chapter 1

Understanding and Applying Single Tip Plasmonics

As discussed in the theoretical background (section **??**) there has been little work to characterise and understand tips prior to applying them as near-field antennae. This has been one of the major driving forces/motivations of this project. For this reason hyperspectral imaging is applied to laterally map the scattering from a tip with spectral confocally localised to infer a local optical response. Understanding the properties of this response at the tip apex of single tips is not only important to determine how they will behave as near-field enhancers but also important in understanding their behaviour in the presence of another tip. By identifying the localised plasmonic behaviour of a set of tips, and comparing it with the underlying geometry, a better understanding can be gained when monitoring the hybridisation process.

1.1 Optical Characterisation of Nanostructures using Hyperspectral Imaging

To optically characterise a sample, it is scanned in a grid under the laser spot and the spectral content of the sampling volume is measured at each point using a spectrometer instead of a photodiode or CCD. This is a form of hyperspectral imaging, allowing for the creation of images at a given wavelength or wavelength band. Rather than comprising of 3 RGB colours, each image pixel is digitised into 1044 bins between 400–1200 nm. This is advantageous over regular imaging as more quantitative information can be extracted from an image to the extent that hyperspectral imaging has become commonplace in many widely spread fields, including microscopy [1, 2], astrophysics [3], remote sensing and geology [4, 5], food standards [6, 7], and medical imaging [8–10]. Within each of these fields it has mostly been used to identify the components constituting an image by their spectral signatures.

By using this hyperspectral imaging technique, LSPs can be spatially identified with confocal resolutions below 300 nm ($\lambda/2NA$). The microscope configuration for this technique is shown in Figure 1.1. This approach to hyperspectral imaging has previously been used to

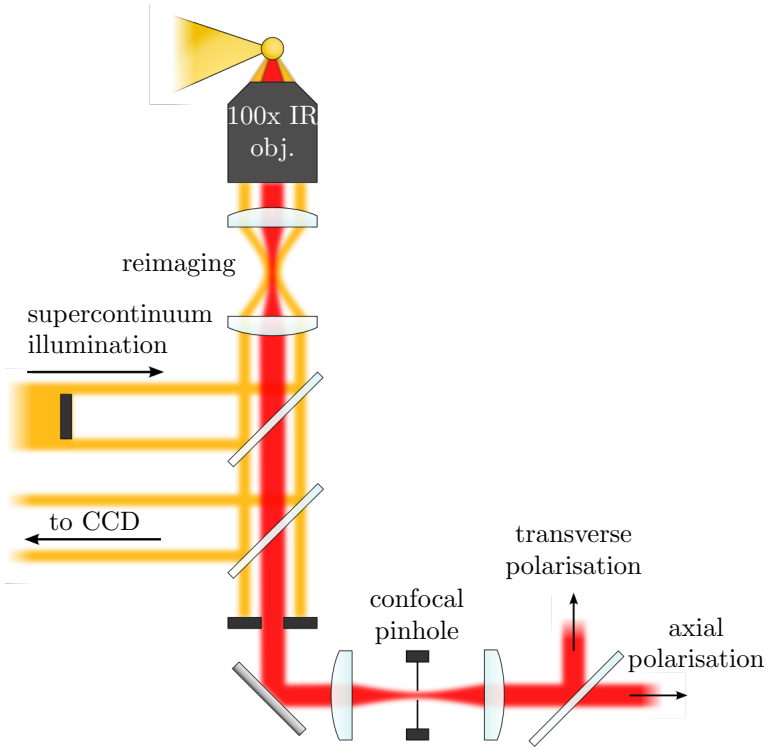

Figure 1.1: Experiment configuration for hyperspectral imaging. The laser is centered on the tip apex for imaging. The tip is scanned across the beam in a grid with spectra acquired at each position. The resulting image then contains 1044 colours at each pixel instead of the usual 3 (RGB).

identify plasmonic modes in aggregated AuNP colloids [11] and to image SPPs [12]. In this experiment the technique is used to study the optical response of sharp and nanostructured tips. It is also used with AuNPs to measure the microscope PSF and map aberrations.

Fast image acquisition is made possible by utilising the ultra-high brightness of a supercontinuum laser source and sensitive, TE-cooled, benchtop spectrometers with a 10 ms integration time. Image acquisition is then limited only by the integration time at each pixel and the ∼30 ms movement time between pixels. During this time the focal intensity is $\sim 10^8$ mW cm^{-2}, which is not sufficiently high enough to damage the 50 nm metallic tip coatings. The illumination and collection configuration is fixed (using the reference intensity) between different samples to maintain comparable scans. Measured spectra are normalised to a spectrum of flat metal of the same material to show geometrical effects only. By using this approach spectral changes between the apex of a tip and its bulk surfaces can be determined.

While not the fastest or most advanced method of acquiring hyperspectral images, the spatial scanning technique is efficient when used with a supercontinuum white-light source, similar to the laser requirement for confocal imaging. Other imaging techniques have been developed to produce hyperspectral images depending on the imaging requirements. These fall under the categories of "spectral scanning", "non-scanning" and "spatio-spectral scanning". Spectral scanning involves wide-field imaging through a range of bandpass filters [13], tuneable

liquid crystal filters [14, 15] or an etalon [16]. This is appropriate if studying large areas or when an increased resolution and improved contrast, gained through confocal optical sectioning, are not required. Similarly, if the benefits of sectioning are not necessary and an imaging spectrograph (monochromator with CCD) is available then only a 1d line scan over the sample is required to form an image as opposed to a 2d grid scan whilst measuring pixel spectra [1]. Non-scanning or snapshot hyperspectral imaging techniques are more complex than the previous two categories as both the spatial and spectral information are acquired in a single measurement without the need for any pixel scanning or dynamic filtering. The main method to achieving this is to use a computed tomography imaging spectrometer (CTIS) [17–20]. By using a 2d dispersive grating in the Fourier plane an image can be split into many spectral images, which can be recorded on a CCD array. Advantages of this approach are short exposure times but necessitates a higher computational requirement to disentangle the 2d image into a cube of dimensions (x, y, λ).

Despite the potential improvements gained by using a more advanced hyperspectral imaging technique, spatial point scanning is deemed the most appropriate solution for characterisation. The imaging process is not time-constrained since the microscope platform is stable, resulting in minimal artefacts due to sample motion, and the use of confocal imaging benefits the acquired image quality. Portable bench-top spectrometers are already incorporated into the microscope for use in other experiments and are readily accessible, therefore adapting the microscope to enable use of an imaging spectrograph and line scanning is not a convenient solution. Wide-field imaging is not beneficial at the set magnification due to the small areas of the overall diffraction-limited image that are point scanned and spectrometers have a far superior spectral resolution compared with imaging through bandpass filters. For these reasons, despite its simple and somewhat relatively slow nature, spatial point scanning is used for characterisation.

1.2 Understanding Plasmon Modes in a Spherical Nanoparticle Tip

To effectively investigate/understand the plasmonics of nanostructured tips, hyperspectral images are taken of four different AFM probes. AFM tips studied are Au- and Pt-coated standard AFM probes (BudgetSensors), 300 nm Au-coated NanoTools B150 AFM probes (spherical tips) [21] and AuNP-on-Pt AFM probes, fabricated in-house using electrochemical deposition [22]. SEM images of these tips are show in Fig. 1.2. Fabricated tips are pre-treated where possible prior to use with ambient air plasma and/or piranha solution to remove organic surface residue and, in some cases, smooth surface roughness.

Comparisons between spherical- and sharp-tipped probes using hyperspectral image slices

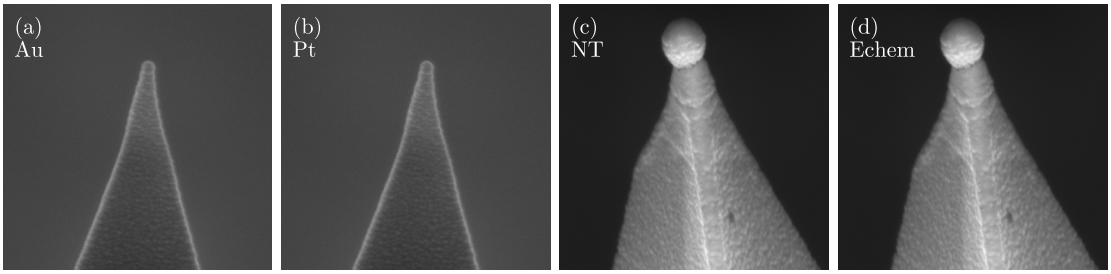

Figure 1.2: SEM images of sharp and spherical metal tips studied using hyperspectral imaging. Tips are (a) a sharp Au AFM tip, (b) a sharp Pt AFM tip, (c) a NT Au-coated spherical AFM tip and (d) an electrochemically deposited AuNP-on-Pt AFM tip.

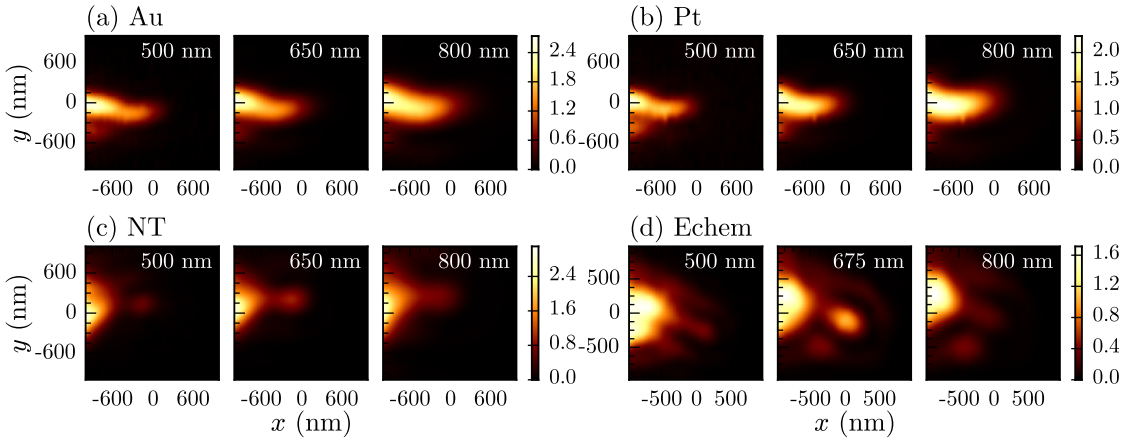

Figure 1.3: Hyperspectral images of sharp and spherical metal tips at wavelengths of interest. Images are of (a) a sharp Au tip, (b) a sharp Pt tip, (c) a NanoTools Au-coated spherical tip and (d) an electrochemically deposited AuNP-on-Pt tip. Collection polarisation is along the tip axis. Colour maps between slices all have the same normalisation. Scattering from the spherical apex is clearly seen in the hyperspectral images of between 600-700 nm.

(Fig. 1.3) show that spherical tips exhibit a characteristic red (600-700 nm) scatter, delocalised from the bulk tip. No similar localised scattering is seen for sharp Au or Pt tips in the visible spectrum, which have an overall weaker optical response. This delocalised apex scatter is typically seen much clearer than when observed in conventional widefield microscopy (Fig. **??**(inset)/(a)). SEM images confirm that this glow occurs only with spherical tip shapes, or when a AuNP is securely attached at the tip apex with a sufficiently small neck joint.

Spectra of tip apices clearly show a structural resonance excited in spherical tips with no obvious resonances present in sharp tips (Fig. 1.4). Apex scatter of spherical tips is strong enough relative to bulk of the tip that it is easily observable with conventional dark-field microscopy superimposed onto the bulk background scatter (Fig. 1.5). These scattering resonances around 630 nm are reliably present in all spherical-tipped probes, both vacuum-processed and electrochemically deposited AuNP-on-Pt, and are attributed to direct LSP excitation. The response of sharp Au tips show no plasmonic features while the slow rise in scattering towards the NIR is consistent with lightning rod scattering [23].

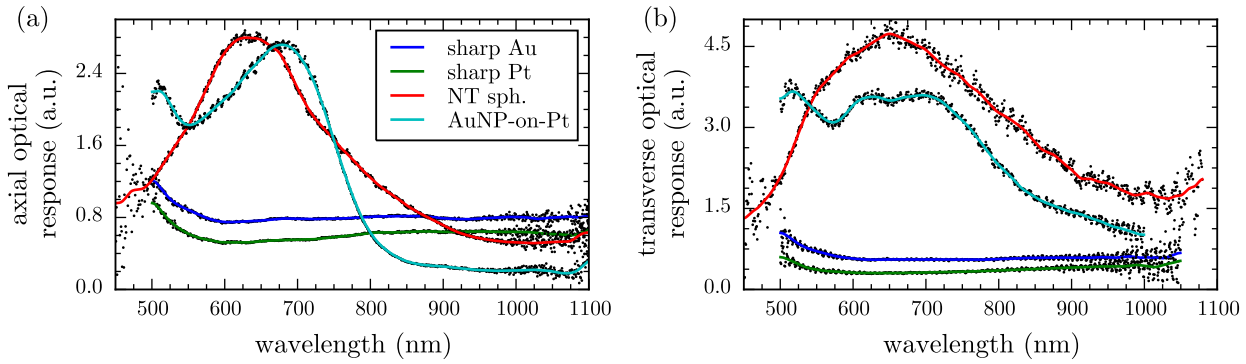

Figure 1.4: Apex spectra of sharp and spherical metal tips. Spectra are extracted from the hyperspectral images in Fig. 1.3 by integrating pixels around the apex region. A clear resonance at 630 nm is observed with spherical tips in both polarisations. The axial/longitudinal tip resonance is blueshifted 20 nm from the longer transverse resonance. Sharp metallic tips show comparatively flat spectra.

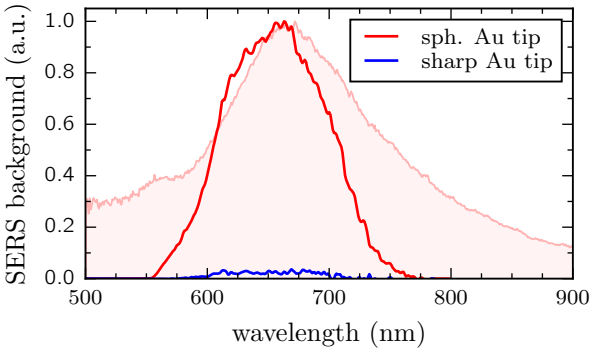

Figure 1.5: Integrated inelastic electron fluorescence measurements of both a sharp and spherical Au tip. Fluorescence spectra are acquired using tuneable, single wavelength spectroscopy with integrated spectra plotted as a function of excitation wavelength. The background spectrum is the supercontinuum dark-field scattering spectrum of the spherical Au tip apex, as measured using hyperspectral imaging. Agreement between the fluorescence (near-field) and dark-field scattering (far-field) spectra confirms resonant near-field enhancement as a localised surface plasmon (LSP) excitation. Sharp Au tips show no such resonance in either the near-field or far-field.

Tuneable single wavelength spectroscopy (fluorescence/Raman spectroscopy) is used to confirm that the resonance is indeed a LSP by showing that the near-field is resonantly enhanced []. Weak near-field processes such as fluorescence and Raman scattering can be plasmonically enhanced and therefore detectable in the far-field. By tuning the laser wavelength and corresponding long-pass filter cut-off wavelength the plasmonic enhancement of near-field processes can be directly observed (Fig. 1.5). Summation of the scattering counts at each excitation wavelength shows a distinct peak around the scattering resonance from Fig. 1.4, confirming it as a LSP resonance. Further, confirmation comes from direct observation of plasmon coupling between spherical tips, previously reported [21].

Surprisingly, the overall disorder and parasitic edge AuNP nucleation on AuNP-on-Pt only minimally effects the overall optical response from the apex growth. Moreso, the AuNP-on-

Pt structure behaves very similar to the Au-coated diamond-like-carbon spherical tip, likely because the 50 nm coating thickness is greater than the skin depth [24, 25]. Plasmons therefore see both as solid Au spheres. Differences arise due to the differences in neck material with Au-Pt and Au-Au neck boundaries.

1.3 Discussion

The plasmon modes of a spherical tip are not so different from those of a sphere/AuNP and can be explained accordingly. Like AuNP plasmons, spherical tip LSPs are specifically *radiative* antenna modes, those that can efficiently couple far-field light with the near-field without the need for momentum matching due to SPP dispersion. On the contrary, LSPs have constant dispersion and require excitation at the resonant wavelength. Radiative antenna LSP modes form only when two close dielectric surfaces surround a metallic particle, allowing the formation of confined multipolar charge oscillations. The resonance wavelength of these modes depends heavily on the spacing between each of the metal/dielectric interfaces, as is observed in the polarisation anisotropy in rod-like or ellipsoidal nanoparticle spectra [26, 27].

Spherical metal tips retain some of the back hemisphere around the connection to the base tip apex, known as the neck region, allowing the spherical apex surface to sustain (multipolar) antenna-like plasmons. Sharp tips do not have this back surface, hence cannot support such resonances. Their metal-dielectric surface still, however, supports the launching of SPPs in the near-field if the coupling/launching conditions are satisfied. The requirement for evanescent coupling means that while a sharp tip can be considered an optical antenna its supported modes are considered as *evanescent* or *near-field* modes rather than *radiative* antenna modes.

Numerical simulations of the near-field around spherical tips, computed using BEMAX, show the plasmon modes of a 250 nm spherical Au tip. The modes of Au and AuNP-on-Pt spherical tips with 100 nm neck diameters are shown in Fig. 1.6(a). Corresponding field enhancement spectra, calculated as the sum of the near-field, are shown in Fig. 1.6(b). A neck width of 0.4 times the sphere diameter (100 nm in this case) is used to match with typical experimental structures. Clear plasmon resonances for both Au and AuNP-on-Pt are found in the calculations with the dominant mode between 600–700 nm agreeing with experimental far-field scattering. From the near-field it is clear that the 600–700 nm SPR in spherical Au tips has a quadrupolar distribution while the longer wavelength dipolar mode exists between 850-1000 nm. Other resonances in the near-field, such as those localised solely around the neck crevices, do not fulfil the antenna conditions and therefore do not couple with light. The dipolar mode shows a strong field at the apex but little field around the rear suggesting it should also be significantly reduced in intensity or even dark, explaining why it is not optically observable.

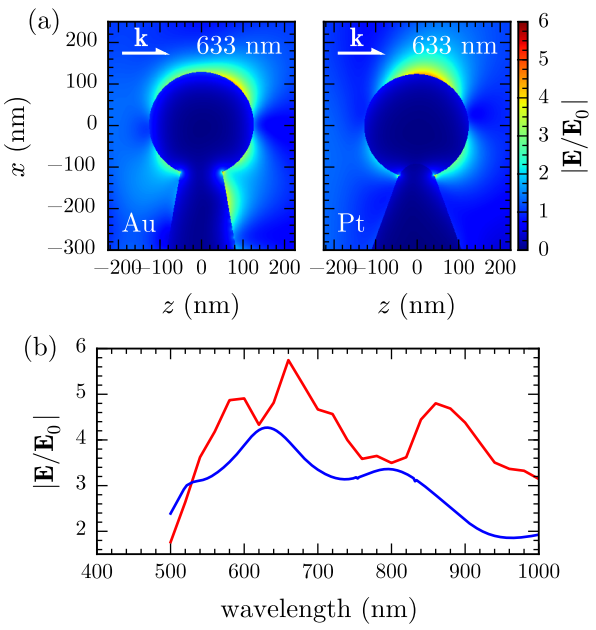

Figure 1.6: Numerical simulations of the field enhancement around a spherical Au tip. (a) Numerical simulations of the near-field around a spherical Au tip and a AuNP-on-Pt tips, both with 250 nm sphere diameters and 100 nm neck diameters. (b) Field enhancement as a function of wavelength, calculated as the summation of the near-fields are shown in (a).

Replacing the Au base tip with a Pt tip replicates the electrochemically-deposited AuNP-on-Pt tips and changes the mode structure. The mode around 630 nm becomes more dipolar in its near-field distribution.

The dependence of the modes and field enhancement on the width of the neck is investigated by widening the neck region until the back surface of the spherical tip disappears. The tip structure therefore transitions from a AuNP until the morphology resembles that of a sharp tip, albeit with a large radius of curvature. The plasmonic contribution of the spherical tip is therefore able to be quantified independent of the lightning rod contribution, which remains constant between all geometries.

Increases in the neck diameter cause a strong blueshift of the dipolar mode from 1000 nm to 850 nm (Fig. 1.7). The quadrupolar mode is far less susceptible to changes in the neck region and therefore does not shift. This explains the robustness of the observed spherical tip plasmon regardless of tip morphology.

The importance of this change is that the largest fields are located at the apex surface along the tip axis, meaning that any surface sees the maximum possible field enhancement. In the case with a spherical Au tip the near-field distribution is quadrupolar which means that the region of maximum field enhancement can never reach the area underneath the AFM tip.

From the presented results we can say that it is important to first consider what plasmons might exist in a particular geometry and the illumination conditions/polarisations required

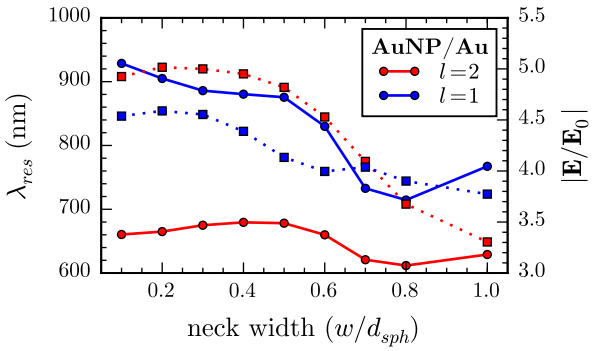

Figure 1.7: Resonant wavelength and field enhancement dependence on the neck width. The resonant wavelength (solid lines) and field enhancement (dashed lines) are plotted for the dipolar (blue) and quadrupolar (red) modes of spherical Au and AuNP-on-Pt tips.

to excite the mode. The existence of radiatively coupled LSPs opens up more experimental geometries using only far-field light, such as the side illumination configuration. If only near-field SPPs exist then evanescent wave coupling must be employed. Regardless of the plasmonics and illumination, the sharpness of the probe will always play a role due to the non-resonant lightning rod effect. By understanding the underlying plasmon modes and the required excitation conditions, combined with pre-characterisation of tips, the field enhancement of tip-based nano-spectroscopy can be optimised/maximised. Through correct nanostructuring of the apex, modes can be tuned across the visible spectrum and brought into resonance with available laser wavelengths. When characterising probes it is necessary to consider an applicable spectroscopy technique. Spectral peaks or shifts from tips observed using wide-field techniques cannot be guaranteed to be localised to the apex. By utilising hyperspectral confocal imaging, with its higher resolution, radiative antenna modes can be locally probed. Furthermore, tuneable single wavelength spectroscopy identifies only features that enhance near-field processes whilst rejecting all other reflections or back-scattering. A significant result of pre-characterising tips is the direct observation that nanostructuring a tip with a sphere gains the tip a robust, far-field coupled apex plasmon around 633 nm. The field enhancement on resonance is sufficient enough for TERS measurements [22, 28]. This both relieves the requirement of near-field excitation and allows one to use readily available HeNe or diode lasers.

As is typically employed in SERS, the degree of confinement/localisation of hotspots is increased through the formation of gap modes between two plasmonic surfaces, increasing the local field enhancement. If the gap modes comprise of at least coupled antenna mode the gap is accessible from the far-field. This allows plasmon coupling to be directly observed experimentally and monitored as a function of gap size [21]. In such cases where the lateral width of the gap mode [29] is small, as is typically the case with nm-scale gaps, the plasmonic contribution will outweigh a lightning rod contribution [], hence spherical tips have the capa-

bility of outperforming much sharper tips. Spherical tips are particularly optimised for use in this configuration since its coupled mode becomes resonant with 785 nm laser light typically found on Raman microscopes for gaps below 2 nm []. Sharp tip TERS tends to use a 488 nm wavelength, likely due to the intrinsic increase in bluer light Rayleigh scattering off the sharp point.

The use of radiative antenna modes in nanostructured tips bridges the gap between SERS and TERS structures. Some of the largest enhancement factors recently measured in plasmonic systems originate from antenna modes in NPs coupled with the charge distribution of their image in a mirror [30, 31]. These systems repeatedly produce Raman/field/intensity enhancement factors of up to 10^7, much like tips, with mode volumes of coupled plasmons on the nm-scale. These systems demonstrate that a plasmonic gap mode can exhibit large field enhancement without requiring contribution from the lightning rod effect. However, the static nature of the NPoM geometry lacks the ability to chemically map a surface. By coupling plasmons in spherical tips with their mirrored image charge a surface could be dynamically mapped with a potentially large field enhancement.

In conclusion, we show that localised surface plasmons can be clearly observed in extended nanostructures using a scanning-confocal hyperspectral imaging in a supercontinuum dark-field microscope. This enables plasmon-dependent applications, such as TERS, to pre-screen nanostructured tips to better improve the reliability and reproducibility of such techniques. Using this technique, the optical/scattering response of spherical-tipped AFM probes is shown to exhibit resonances not present in standard metallic AFM probes. Observed resonances correspond to antenna modes of the system, those which couple readily with light without the need for momentum matching. These modes determine what plasmonic phenomena are able to be experimentally observed, hence spherical tips can be used to dynamically investigate plasmonics.

1.4 Non-Plasmonic Performance of Spherical Au Nanoparticle Tips

The conductive Au-coating on the spherical tips means they can be used both with the capacitive tip alignment technique and also for measuring current through a tip dimer nano-gap.

Figure 1.8: Comparison of alignment scans using sharp Au tips and spherical Au tips. The width of the peak in the alignment scans is limited to the apex diameter. The peak width when aligning spherical Au tips is therefore much larger than when aligning sharp Au tips.

Fabricated AuNP-on-Pt tips perform similarly to vacuum-processed spherical Au tips during tip alignment using scanning capacitance microscopy. As the AuNP is grown directly onto

the Pt the spherical apex remains highly conductive. A high conductivity is ensured during experiments by cleaning the tips prior to use to remove any insulating surface contaminants.

1.5 Improved Field Enhancement of Spherical Au Nanoparticle Tips

A result of spherical Au tips sustaining plasmon resonances which couple with the far-field is that their plasmonic contribution to the field enhancement can outperform the lightning rod contribution in sharp tips (assuming no near-field plasmonic excitation in sharp tips). The field enhancements for both sharp and spherical Au tips, more specifically the fabricated AuNP-on-Pt tips, are determined in a far-field side illumination configuration by using Raman scattering.

Supercontinuum dark-field spectroscopy is used in conjunction with Raman spectroscopy in a modified version of the microscope platform, enabling both techniques. Fabricated AuNP AFM tips are mounted opposite a benzenethiol-coated sharp Au AFM tip in a tip-to-tip configuration, mimicking a plasmonic bow-tie antenna (Figure 1.9). This configuration is used to obtain good optical access to the dimer gap for spectroscopically probing its plasmonic properties. Benzenethiol (BTh) is used as a Raman marker for measuring the relative field enhancement of AuNP tips due to its strong Raman response and well-known spectra [32, 33]. BTh (VWR International Thiophenol for synthesis) is diluted to 5 mM solutions into ethanol (Sigma-Aldrich). Tips for use as SERS substrates are prepared by coating a monolayer of BTh onto the surface. This is achieved by submerging a standard Au-coated AFM tip in 100 mM ethanolic BTh solution for 1 min followed by rinsing with ethanol and drying in nitrogen. This

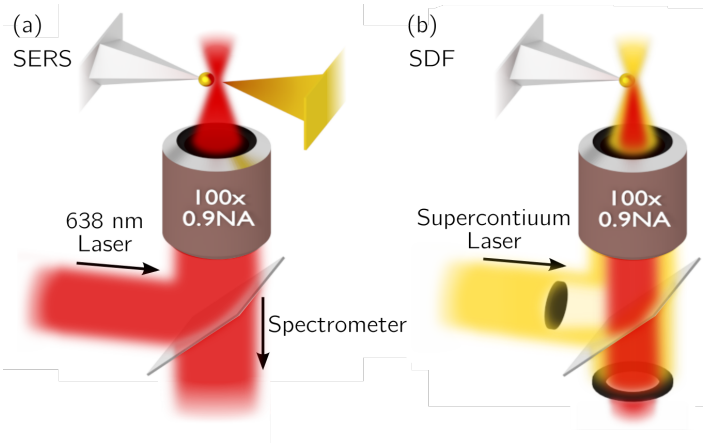

Figure 1.9: Experimental geometry for dark-field spectroscopy and SERS measurements. A 125 nm radius spherical AuNP grown onto a Pt-coated AFM tip is spectroscopically studied using a supercontinuum laser in a dark-field configuration. The tip is then brought within 1 nm of a benzenethiol-coated sharp Au tip under 638 nm illumination to measure SERS spectra.

is repeated 5 times to ensure complete monolayer coverage. Tips for use as plasmonic probes are not coated in BTh.

With the BTh tip retracted, dark-field apex scattering spectra of tips is acquired using the supercontinuum laser source. After characterisation the microscope optics are modified into a TERS configuration and the plasmonic probe tip is aligned to the BTh tip using the capacitive tip alignment technique.[1] Once aligned, the gap size is reduced to ∼1 nm, limited by the thickness of the assembled BTh molecular layer, and illuminated through a 100× 0.9 NA visible objective with 3 mW (1.9 MW cm^{-2}) of 638 nm laser light incident on the gap, polarised along the tip axis. Scattered light is collected through the same objective and confocally localised. Raman spectra are filtered using a 650 nm long-pass filter prior to dispersion in a spectrometer. Contact dynamics, confirming that tips come into physical contact, while separated by a BTh layer are measured using in-built AFM laser deflection from the cantilever of the approaching tip.

Near-field calculations for the spherical Au tip are computed for comparison with experimental results and to understand the enhancement mechanism. The near-field distribution at 633 nm and the spectrum 1 nm from the apex are calculated using the full electrodynamic boundary-element method [34, 35].[2] The spherical tip is modelled as a Pt cone with half-angle 20° with a 250 nm diameter AuNP attached to its end. The neck radius between sphere and tip is 50 nm. The tip is illuminated with a plane wave polarised along the tip axis.

A 125 nm radius spherical AuNP-on-Pt tip, grown as described in section **??** (−8 V, 150 ms exposure), is used to demonstrate the augmented plasmonic properties of spherically nanostructured tips. Raman spectra of BTh molecules in the tip dimer gap are greatly enhanced when using a AuNP tip in place of a sharp Au tip (Figure 1.10a). As the same spectrometer is used for both broadband scattering spectra and SERS spectra, its restricted spectral resolution (300–1100 nm bandwidth), combined with the broadness of the diode laser line illumination, blurs the characteristic multiple Raman peaks of BTh between 1000–1600 cm^{-1}. However the resulting observation of two broad peaks in this region affirms the presence of BTh in the gap between tips. The background signal is also enhanced across a broad bandwidth, as is typical for SERS [32].

Supercontinuum dark-field scattering spectra (Figure 1.10b), taken of individual tips prior to SERS measurements, show that the increased Raman enhancement when using a AuNP tip is due to excitation of a LSP around 630 nm, not present in sharp Au tips. This is in good agreement with boundary element calculations of the near-field enhancement at the AuNP tip apex with a visible plasmon resonance observed across the AuNP (Figure 1.10b,c). Coupling between this LSP in the AuNP tip with a BTh-coated sharp Au tip forms a confined gap plasmon mode. Since coupling is between higher order modes in the sharp Au tip, shifting

[1] The optics are modified in the sense that the laser input is switched and the dark-field iris is opened.
[2] Near-field calculations carried out by Lars O. Herrmann.

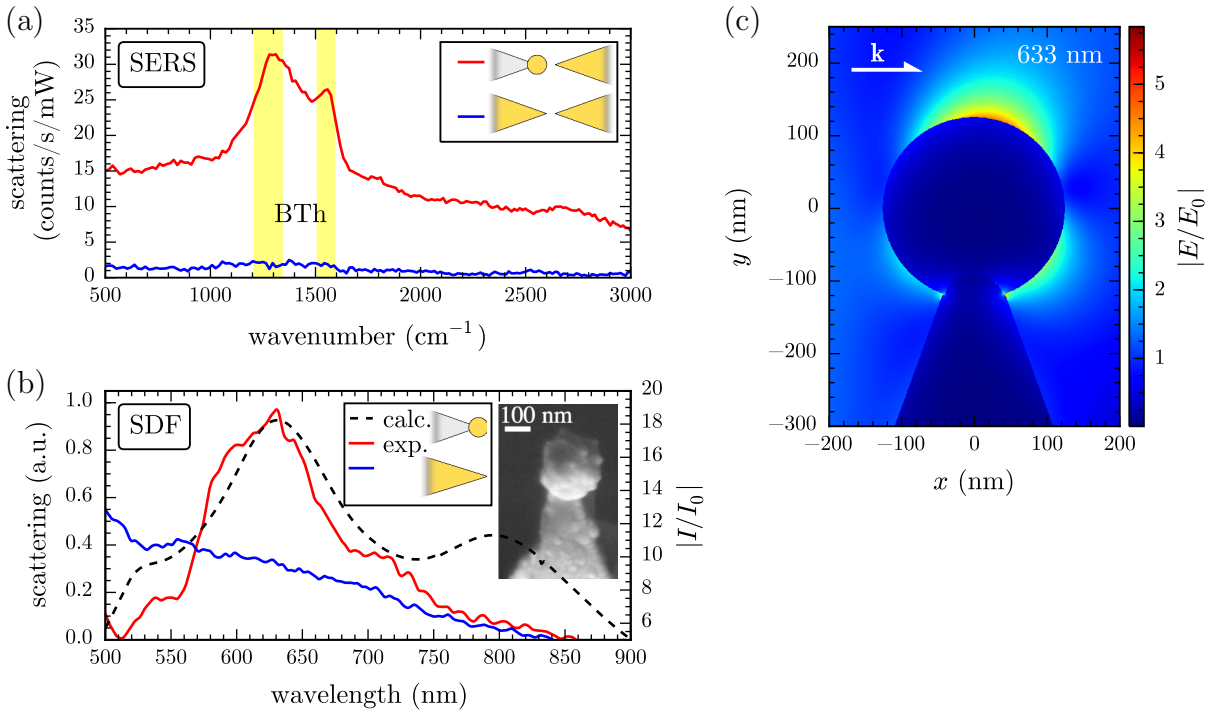

Figure 1.10: Application of sharp Au and AuNP-on-Pt tips to enhancing Raman scattering. (a,b) Comparative TERS and dark-field spectroscopy of sharp Au and AuNP tips. (a) Tip-enhanced Raman spectra of a benzenethiol-coated Au AFM probe brought close to the AuNP tip (red), compared to a sharp Au AFM tip (blue). (b) Dark-field optical scattering of AuNP (red) and sharp Au (blue) AFM tips, with calculated relative intensity enhancement 0.5 nm from the AuNP tip apex (dashed). The inset shows an SEM image of the 125 nm AuNP tip. (c) Calculated field enhancement profile for a 125 nm radius AuNP at the end of a 1500 nm long Pt tip. The neck join is 50 nm wide and the tip is under longitudinally polarised plane wave illumination at 633 nm.

of this resonance as a function of gap size is weak [36].[3] Illuminating on resonance with the plasmon therefore greatly increases the Raman response by a factor of 30. This corresponds to a relative SERS enhancement of 12 when using a AuNP tip as opposed to a sharp Au tip after taking into account the confinement and mode volume of a LSP to the gap in each case [29]. Since the LSP is laterally confined to only 7 nm within this gap the enhanced Raman signal is the result of scattering contributions from only a very small number of molecules. This leads to lower bound estimates for the absolute SERS enhancements of 1.9×10^5 for the AuNP tip and 1.6×10^4 for a sharp Au tip. Though absolute estimates are not as high as expected, the relative SERS enhancement observed with the AuNP tip is indeed comparable to previously reported results [28].

Field enhancements are estimated by first calculating the mode volumes of plasmonic gap modes. The lateral width of a gap plasmon mode is given by $w = \sqrt{R_{\text{eff}} d}$, where R_{eff} is the effective radius of the particles, $\sqrt{R_1 R_2}$, comprising the plasmonic dimer and d is the width

[3] This needs checking

of the gap separating particles [29].[4] This results in lateral mode widths of 4.5 nm for the sharp Au tip of 20 nm radius and 7.1 nm for a 125 nm AuNP tip.[5] Assuming a cylindrical gap mode yields mode volumes of 15.7 nm^3 and 39.3 nm^3, respectively. These define the near-field contribution to Raman scattering and a relative field enhancement is obtained using,

$$FE_{real} = \frac{N_{AuNP}/V_{AuNP}}{N_{tip}/V_{tip}} \tag{1.1}$$

where N is the Raman signal counts and V is the mode volume. This evaluates to 12. Lower limit absolute field enhancements are estimated using,

$$FE_{abs} = \frac{N_{near-field}/V_{near-field}}{N_{far-field}/V_{far-field}} \tag{1.2}$$

where $N_{far-field}$ is assumed to be 0.1 counts/s/mW from the noise levels since signals are below the signal to noise level and $V_{far-field}$ is assumed to be 25 000 nm^3 based upon the surface of a conical tip exposed to the focal volume of a diffraction limited spot ($d = 412$ nm at $\lambda = 638$ nm). This expression yields absolute field enhancements of 1.9×10^5 for an 80 nm AuNP tip and 1.6×10^4 for a sharp Au tip.

These optical measurements confirm that AuNP tips provide increased field enhancement compared to sharp Au tips due to a strong LSP excitation. Lack of any strong peaks around 600 nm in dark-field spectra of sharp Au tips suggest that any plasmons present are weakly coupled and do not scatter strongly in this illumination geometry. Such plasmons may still couple with the opposing tip to form a gap mode but reduced localisation results in a lower field enhancement. On the other hand, AuNP tips are well suited to high enhancements when illuminated at the appropriate plasmonic resonances. Whilst a number of plasmonic probes have been developed recently, several useful features are obtained here. By using standard AFM probes as a basis, these AuNP tips maintain their functionality as AFM probes for force microscopy, as demonstrated by the alignment of tips using resonant capacitive driving. The metallic coating of these tips also allows for simultaneous electrical measurements whilst performing optical and AFM force measurements. These tips therefore function as standard electrical AFM probes with added plasmonic functionality. Furthermore, such tips also show excellent resistance to damage at the tip apex after multiple surface contacts, though surfaces do become deformed after heavy use. Their robust nature is attributed to the direct growth of the AuNP root across the pyramidal tip end. This is a significant improvement over currently-available commercial spherical AFM tips, in which the spheres break from the tip and adhere to the contact surface after only one or a small number of contact cycles.

[4] The use of $R_{\text{eff}} = \sqrt{R_1 R_2}$ is justified by...

[5] Note that these widths are below the quantum limit for such large AuNPs only because the opposing tip has such a small radius to increase localisation.

Several advantages emerge from apex-selective single nanoparticle electrochemical growth. Simultaneous nanoparticle growth on many tips ensures a high throughput process, while morphology and size is controlled by voltage and time. This provides a viable method for producing tips capable of expanding the user-base of plasmonics and furthering research into applications of TERS and SNOM. Further applications are envisaged, for instance in plasmonic optical trapping [37] because the tips in the present geometry can conveniently act as a heat sink reducing the problematic optical heating observed, and resulting thermal damage. Furthermore, the spherical nanoparticle growth method introduced here is not restricted to specific metals, and many different composite systems can be created with this apex-localised growth technique. For example silver nanoparticle tips give a larger optical response and field enhancement under visible illumination (although oxidation is sometimes an issue).

1.6 Understanding the SERS Mechanism: Tuneable Raman on Spherical Au Tips

Previously we have shown that spherical Au tips possess strong far-field antenna LSPs and that the Raman enhancement is higher than for a sharp tip. By utilising this resonance it becomes possible to map the SERS background as a function of excitation wavelength around the plasmon.

A tuneable pulsed laser, outputting wavelengths between 500 nm – 700 nm, is used in conjunction with an individual tip to understand the link between the localised plasmon resonance and the SERS mechanism.[6] By measuring the SERS background, known to be caused by inelastic scattering of internal free electrons in the metal [38], at various excitation wavelengths and comparing with a scattering spectrum of the plasmon, the enhancement mechanism can be uncovered.

The electromagnetic enhancement of SERS is widely believed to be due to plasmonic enhancement of the intrinsic inelastic scattering []. The simple mechanism by which the plasmon enhances the field is described below.

The intensity from inelastic scattering of light, also known as Raman scattering, can be described by,

$$I_{scat}(\omega) = P(\omega - \omega_0) I_{in}(\omega_0), \tag{1.3}$$

where the outgoing scattering, I_{scat} at a given frequency, $\omega = \omega_0 - \delta\omega$ is proportional to the amount of incident light, $I_{in}(\omega_0)$ where only a fraction of photons, $P(\omega - \omega_0)$, are inelastically

[6] Tuneable Raman setup built by Anna Lombardi and Lee Weller. SERS background measurements carried out by Anna Lombardi.

scattered. The intensity goes as the $\mathbf{E}^2$ hence (1.3) can be expressed as,

$$I_{scat}(\omega) = |\mathbf{E}_{scat}(\omega)|^2 = P(\omega - \omega_0)\,|\mathbf{E}_{in}(\omega_0)|^2\,. \tag{1.4}$$

The SERS mechanism, in its simplest form, can be described resonant near-field enhancement, or mode coupling, of both the incident field, $\mathbf{E}_{in}(\omega_0)$, and the outgoing scattered field, $\mathbf{E}_{scat}(\omega)$. This process is be described in the relations,

$$\mathbf{E}_{in}(\omega_0) = \mathbf{g}(\omega_0)\mathbf{E}_{in,0}(\omega_0), \tag{1.5a}$$
$$\mathbf{E}_{scat}(\omega) = \mathbf{g}(\omega)\mathbf{E}_{scat,0}(\omega), \tag{1.5b}$$

where $\mathbf{g}(\omega)$ is the plasmon resonance enhancing the initial fields $\mathbf{E}_0$. The plasmon gain is a vector to account for the polarisation response of the field enhancement. Substituting the enhanced fields back into (1.4) yields firstly that,

$$I_{scat}(\omega) = |\mathbf{E}_{scat}(\omega)|^2 \tag{1.6}$$
$$= \mathbf{g}^2(\omega)\,|\mathbf{E}_{\mathbf{scat,0}}(\omega)|^2\,, \tag{1.7}$$

the scattered intensity is enhanced by $\mathbf{g}^2(\omega)$, and secondly that,

$$\mathbf{E}_{scat,0}(\omega) = P^{1/2}(\omega - \omega_0)\mathbf{E}_{in}(\omega_0) \tag{1.8}$$
$$= P^{1/2}(\omega - \omega_0)\mathbf{g}(\omega_0)\mathbf{E}_{in,0}(\omega_0), \tag{1.9}$$

the incident field is also enhanced by a similar factor $\mathbf{g}(\omega_0)$. Factoring out the bare Raman signal, $I_{scat,0}$, as given in (1.4), results in the complete SERS signal,

$$I_{scat}(\omega) = \mathbf{g}^2(\omega)\left|P^{1/2}(\omega - \omega_0)\mathbf{g}(\omega_0)\mathbf{E}_{in,0}(\omega_0)\right|^2, \tag{1.10}$$
$$= g^2(\omega)g^2(\omega_0)I_{scat,0}. \tag{1.11}$$

From this we see that the original Raman signal is enhanced by a factor $g^2(\omega)g^2(\omega_0)$. For illumination wavelengths just below the plasmon resonance, when $g(\omega_0) \approx g(\omega_{scat})$, the enhancement of Raman scattering goes as g^4. Hence the weak near-field Raman scattering is now efficiently transmitted into the far-field, resulting in an orders of magnitude signal increase when measuring in the vicinity of a plasmonic surface.

Inelastic/Raman scattering spectra showing the broad SERS background at excitation wavelengths between 500 nm – 700 nm are shown in Figure 1.11a along with the plasmon spectrum in Figure 1.11b, as measured using supercontinuum dark-field spectroscopy. The square root of the plasmon spectrum is interpolated to form the plasmon gain function $g(\lambda)$. The

(a) Scattering spectra showing the SERS background from a spherical Au tip at various excitation wavelengths. Spectra are acquired by integrating for 10 s at 10 µW incident powers.

(b) Supercontinuum dark-field scattering spectrum of the spherical Au tip used to measure the SERS background. The overlaid line is the interpolated plasmon function.

Figure 1.11

SERS model from (1.11) is multiplied by a factor $\left(1 - e^{-c(\lambda_{scat} - \lambda_{ex})}\right)$ to model the experimental cut-on of the long-pass filter. SERS backgrounds modelled using (1.11) and the experimental gain function are shown in Figure 1.11b. Both experiment and model at first show good agreement. The shape of the SERS background follows the shape of the plasmon resonance to some extent.

Figure 1.12: SERS analysis.

Extracting the wavelength of maximum intensity and integrated counts from each SERS background and plotting against the excitation wavelength shows that the enhancement peaks when illumination is slightly blueshifted from the plasmon (Figure **??**). This is expected as the plasmon maximally enhances both the blueshifted incident light and the redshifted scattered light. Significant deviations occur when comparing the maxima and integrated counts between experiment and model. Experimental data shows a much sharper resonance than accounted for in the model.

1.7 Conclusions

In conclusion, we have demonstrated a simple, fast method for the reliable growth of plasmonic spherical AuNP AFM tips. We showed this capability through measurements of dark-field scattering and SERS on controlled tip dimers at nanoscale separations.

References

[1] R. A. Schultz et al., Cytometry **43**, 239–247 (2001).

[2] S. J. Leavesley et al., Journal of biophotonics **5**, 67–84 (2012).

[3] E. K. Hege et al., in Optical science and technology, spie's 48th annual meeting (International Society for Optics and Photonics, 2004), pp. 380–391.

[4] J. A. Hackwell et al., in Spie's 1996 international symposium on optical science, engineering, and instrumentation (International Society for Optics and Photonics, 1996), pp. 102–107.

[5] G. A. Shaw and H.-h. K. Burke, Lincoln Laboratory Journal **14**, 3–28 (2003).

[6] M. Kim, Y. Chen, P. Mehl, et al., Transactions-American Society of Agricultural Engineers **44**, 721–730 (2001).

[7] A. Gowen et al., Trends in Food Science & Technology **18**, 590–598 (2007).

[8] T. Vo-Dinh, Engineering in Medicine and Biology Magazine, IEEE **23**, 40–49 (2004).

[9] M. E. Martin et al., Annals of biomedical engineering **34**, 1061–1068 (2006).

[10] G. Lu and B. Fei, Journal of biomedical optics **19**, 010901–010901 (2014).

[11] L. Herrmann et al., Optics express **21**, 32377–32385 (2013).

[12] M. Bashevoy et al., Optics express **15**, 11313–11320 (2007).

[13] M. Iga et al., Review of Scientific Instruments **83**, 103707 (2012).

[14] R. W. Slawson, Z. Ninkov, and E. P. Horch, Publications of the Astronomical Society of the Pacific **111**, 621–626 (1999).

[15] N. Gat, in Aerosense 2000 (International Society for Optics and Photonics, 2000), pp. 50–64.

[16] J. T. Daly et al., in Symposium on integrated optoelectronics (International Society for Optics and Photonics, 2000), pp. 104–115.

[17] T. Okamoto and I. Yamaguchi, Optics letters **16**, 1277–1279 (1991).

[18] T. V. Bulygin and G. N. Vishnyakov, in Analytical methods for optical tomography (International Society for Optics and Photonics, 1992), pp. 315–322.

[19] T. Okamoto, A. Takahashi, and I. Yamaguchi, Applied Spectroscopy **47**, 1198–1202 (1993).

[20] M. Descour and E. Dereniak, Applied Optics **34**, 4817–4826 (1995).

[21] K. J. Savage et al., Nature **491**, 574–577 (2012).

[22] A. Sanders et al., Particle & Particle Systems Characterization **32**, 182–187 (2015).

[23] W. Zhang, X. Cui, and O. J. Martin, Journal of Raman Spectroscopy **40**, 1338–1342 (2009).

[24] M. I. Stockman, Optics express **19**, 22029–22106 (2011).

[25] C. Huber et al., Physical Chemistry Chemical Physics **16**, 2289–2296 (2014).

[26] J. Mock et al., The Journal of Chemical Physics **116**, 6755–6759 (2002).

[27] H. Kuwata et al., Applied physics letters **83**, 4625–4627 (2003).

[28] T. Umakoshi et al., Applied Physics Express **5**, 052001 (2012).

[29] I. Romero et al., Optics Express **14**, 9988–9999 (2006).

[30] J. Mertens et al., Nano letters **13**, 5033–5038 (2013).

[31] R. W. Taylor et al., Scientific reports **4** (2014).

[32] S. Mahajan et al., The Journal of Physical Chemistry C **114**, 7242–7250 (2009).

[33] P. V. Dudin, P. R. Unwin, and J. V. Macpherson, The Journal of Physical Chemistry C **114**, 13241–13248 (2010).

[34] F. G. De Abajo and J Aizpurua, Physical Review B **56**, 15873 (1997).

[35] F. G. de Abajo and A Howie, Physical Review B **65**, 115418 (2002).

[36] J. T. Hugall, J. J. Baumberg, and S. Mahajan, The Journal of Physical Chemistry C **116**, 6184–6190 (2012).

[37] N. C. Lindquist et al., Laser & Photonics Reviews **7**, 453–477 (2013).

[38] J. T. Hugall and J. J. Baumberg, Physical Review Letters (2015).